Earth and Planetary Science Letters 402 (2014) 247–256

Contents lists available at ScienceDirect

Earth and Planetary Science Letters

www.elsevier.com/locate/epsl

A comparative study of low frequency earthquake templates in northern Cascadia

A.A. Royer *, M.G. Bostock **

Department of Earth, Ocean and Atmospheric Sciences, The University of British Columbia, Vancouver, BC, Canada

ARTICLE INFO

Article history:
Accepted 19 August 2013
Available online 20 September 2013
Editor: P. Shearer

Keywords:
low frequency earthquakes
tremor
Cascadia subduction zone
moment tensor inversion
plate boundary
intraplate seismicity

ABSTRACT

Using network correlation methods, we generate low frequency earthquake templates for a set of 4 composite arrays on Vancouver Island and Washington state that employ data from EarthScope (Transportable and Flexible Arrays, Plate Boundary Observatory), POLARIS and permanent network (Canadian National Seismograph Network, Pacific Northwest Seismic Network) sources. On the basis of empirical and semi-analytical arguments, the templates can be viewed as Green's function sections corresponding to moment tensor point sources with step-function time dependence in displacement. Low frequency earthquake hypocentres follow the general epicentral distribution of tremor and occur along tightly defined surfaces in depth with Washington locations averaging slightly deeper than those on Vancouver Island. We invert template waveforms for moment tensor mechanisms and find that data are well modelled by double couple sources. For southern Vancouver Island, with the highest quality templates, the majority of mechanisms are consistent with shallow thrusting in the direction of plate motion. The three other data sets with lower signal to noise levels show predominantly thrust mechanisms with more variable orientations. Taken together with other constraints, our observations support the hypothesis that low frequency earthquakes manifest shear slip on a relatively thin plate boundary.

1. Introduction

The discoveries of non-volcanic tremor by Obara (2002) just over a decade ago and its associations with slow slip (Rogers and Dragert, 2003) and low frequency earthquakes (Shelly et al., 2007) have opened many new avenues of study in seismology. Unlike regular earthquakes, the low frequency earthquakes (LFEs) that constitute tremor may repeat 1000's of times over periods of a few years. Despite low magnitudes ($M < 3$) and limited bandwidth (1–10 Hz), these signals can be detected at low signal-to-noise ratio (SNR) thresholds and with high temporal precision using powerful network correlation techniques (Gibbons and Ringdal, 2006; Shelly et al., 2006; Brown et al., 2008). Analysis of LFEs, and tremor more generally, can be facilitated through the generation of high SNR LFE templates assembled by stacking multitudes of aligned, repeating waveforms (e.g. Shelly and Hardebeck, 2010; Bostock et al., 2012; Frank et al., 2013; Nowack and Bostock, 2013). The templates accentuate impulsive body wave arrivals allowing travel times to be measured more accurately, polarities to be determined with greater confidence and waveform distortion and scattered signals related to structure to be identified.

In this paper, we generate LFE templates from tremor recorded in northern Vancouver Island and Washington state, thereby extending a previous LFE catalogue for southern Vancouver Island (Bostock et al., 2012) through much of northern Cascadia. We then provide empirical and semi-analytical arguments justifying the identification of LFE templates with "Green's function" sections corresponding to moment tensor point sources exhibiting a step-function time dependence in displacement. We proceed to compare the distribution and excitation of LFE sources across northern Cascadia as revealed by LFE templates and discuss implications for plate boundary structure and LFE genesis.

2. Data

Data employed in this study were collected from a variety of EarthScope sources that include Plate Boundary Observatory (PBO) short-period borehole installations, the transportable USArray (TA), and the Flexible Array experiments CAFE and FACES. In addition, we also employ data from permanent stations of the Canadian National Seismograph Network (CNSN) and the Pacific Northwest Seismic Network (PNSN), as well as portable POLARIS deployments on Vancouver Island. Data from southern Vancouver Island have been described previously by Bostock et al. (2012) and are

* Corresponding author.
** Principal corresponding author.
E-mail addresses: aroyer@eos.ubc.ca (A.A. Royer), bostock@eos.ubc.ca (M.G. Bostock).

0012-821X/$ – see front matter
http://dx.doi.org/10.1016/j.epsl.2013.08.040

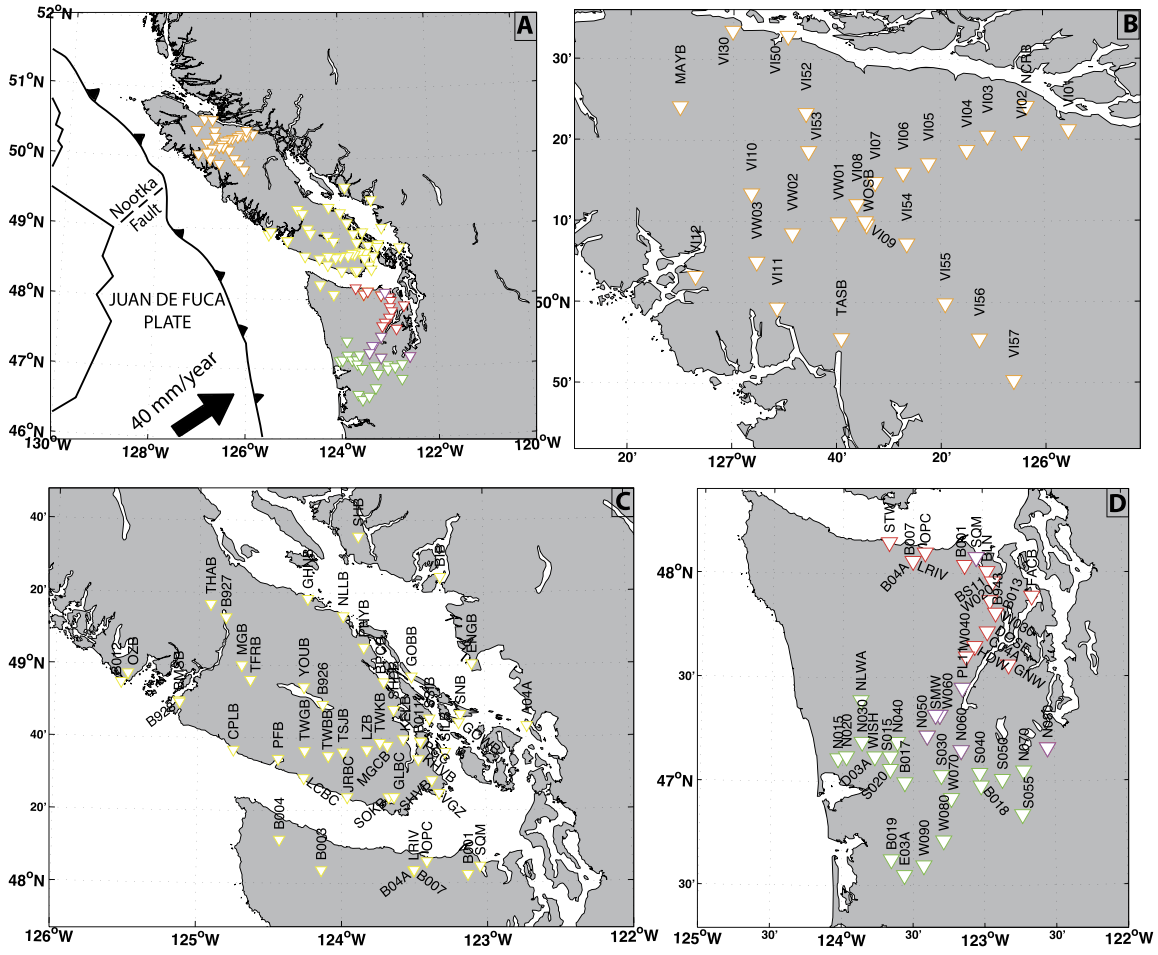

Fig. 1. Distribution of stations used in the study of LFE templates in Washington state and Vancouver Island. Top left panel (A) shows northern Cascadia region including plate boundary and colour-coded station locations (NVI – orange, SVI – yellow, NW – red, SW – green, shared NW/SW – purple). Remaining panels (B)–(D) show map insets of station locations for the NVI, SVI and collective NW and SW subarrays, respectively. (For interpretation of the references to colour in this figure legend, the reader is referred to the web version of this article.)

included in this work for comparative purposes. The full suite of stations are shown in Fig. 1. Data were divided into 4 subarrays, namely northern Washington (NW), southern Washington (SW), northern Vancouver Island (NVI) and southern Vancouver Island (SVI), that were processed independently.

2.1. Washington state

The majority of data employed in the analysis of LFEs in Washington state were collected as part of the Flexible Array CAFE experiment (Abers et al., 2009; Calkins et al., 2011). We separate the dataset into NW and SW components. The former comprises 25 stations skirting the eastern flanks of the Olympic Peninsula to the west of Puget Sound, whereas the latter includes 25 stations running approximately east–west to the southwest of Puget Sound. Fig. 1D displays the distribution of these stations. For the NW dataset, major tremor episodes in 2007, 2008, 2009, 2010 and 2011 were recorded, but only data from the 2007 and 2008 tremor episodes were available for the SW subarray. Episodic tremor and slip episodes such as these typically last up to ∼3 weeks in Washington and southern Vancouver Island (Rogers and Dragert, 2003).

2.2. Vancouver island

Tremor data for the NVI dataset were assembled from a portable POLARIS deployment on northern Vancouver Island that comprised 27 broadband seismometers deployed along two mutually perpendicular arms (Audet et al., 2008), as shown in Fig. 1B. Two tremor episodes in 2006 and 2007 were available for analysis, each episode lasting under 1 week in duration. Analysis of LFEs for SVI relied heavily on a line of some 10 stations extending from the west coast of Vancouver Island (PFB) to the Gulf Islands (SNB) but also incorporated an additional >20 stations from surrounding areas. Tremor episodes in 2003, 2004 and 2005 were recorded at a majority of the stations, but data from subsequent episodes through 2012 have been incorporated for stations as available.

3. Data processing

All data were divided into 24 hour-long segments, band-pass filtered between 1 and 8 Hz, resampled to 40 sps, and subjected to three distinct data processing steps to obtain LFE templates. These steps comprised i) network autocorrelation to identify pairs of repeat LFEs (Brown et al., 2008), waveform-correlation cluster analysis (Rowe et al., 2002) to sort LFE detections into initial templates based on waveform similarity, and iii) network correlation (Gibbons and Ringdal, 2006; Shelly et al., 2006) and stacking to increase detections and improve LFE template SNR. Bostock et al. (2012) provide details on processing of the SVI dataset, so we consider only NW, SW and NVI datasets below.

3.1. Network autocorrelation

For the NW dataset, we applied network autocorrelation to 4 tremor episodes (January 17–30, 2007, May 01–23, 2008, August 07–24, 2010 and August 04–23, 2011) using the 7 three-component stations B001, SQM, BS11, W020, W040, GNW and PL11. For the SW dataset, we performed network autocorrelation using 2 tremor episodes (January 14–February 01, 2007, May 01–25, 2008) and employed the 7 three-component stations N050, S030, W070, N060, PL11, S040 and N070. Network autocorrelation for the NVI dataset was applied to two tremor episodes (September 05–11, 2006, June 13–18, 2007) for different combinations of 7 of the 10 three-component stations VI10, VW03, VI11, VW02, VI52, VI53, VI05, VI08, VI06, VI04.

Each of these data sets was independently analyzed on an hour-by-hour basis. Each hour-long segment was divided into 15 s windows lagged by 0.5 s to produce a total of 7170 individual windows per hour. Each window was correlated with all other windows in the same 1-hour record for an individual (station-component) channel. The resulting time-series from all stations and all components corresponding to the same hour were stacked to create "network autocorrelation" records. When the network autocorrelation exceeded 8 times the median absolute deviation (Shelly et al., 2006), we registered the corresponding window pairs as LFE detections. This catalogue was then culled to exclude overlapping detections and retain only those with high SNR. After processing all data, we had selected 4915, 3306 and 4267 initial detections for further analysis from the NW, SW and NVI datasets, respectively.

3.2. Waveform-correlation cluster analysis

We proceeded to combine all channels corresponding to a given detection into a single "super" trace and cross-correlated all such traces against one another to determine maximum correlation coefficients and corresponding lags. The correlation coefficients were used to populate a similarity matrix employed within a hierarchical cluster analysis, allowing the detection waveforms to be grouped into clusters. Waveforms for all channels (stations/components) available for detections within a given cluster were shifted and stacked to produce an initial LFE template. This procedure resulted in 224, 70 and 54 initial templates for the NW, SW and NVI datasets, respectively.

3.3. Network cross-correlation

Iterative network cross-correlation and stacking was used to register further detections and improve template SNR. We performed network cross-correlation by choosing subsets of 7 to 10 high SNR, three-component stations available within a template and scanning through all available tremor dates. As before, when the summed network cross-correlation coefficient exceeded 8 times the median absolute deviation, now for a 24-hour period, we logged detections. New templates were formed by stacking waveforms (normalized to unit maximum amplitude across three components) for all newly registered detections. After several iterations of network cross-correlation and stacking, we obtained final sets of templates suitable for location and waveform analysis. Our final suites of templates number 122, 54 and 47 for the NW, SW and NVI datasets, respectively. Each template possesses 100's to 1000's of independent detections. Fig. 2 shows examples of LFE templates from each of the NW, SW, NVI datasets.

4. LFE templates as empirical Green's functions

In Fig. 3 we plot P and S waveforms at stations located near the centre of NVI (top panels), NW (middle panels) and SW (bottom panel) arrays. In each panel, waveforms are ordered in increasing epicentral distance (ranging from 1 to 71 km, see the following section) and aligned with respect to the dominant P- or S-arrival. Bostock et al. (2012, Fig. 6) present a similar figure for the SVI data. In contrast to this previous study, we have applied a 90° phase shift (Hilbert transform) to the template waveforms that accomplishes partial transformation from particle velocity to particle displacement without altering the amplitude spectrum. The effects of post-critical scattering interactions that induce complex waveform distortions are minimized for these station selections because the majority of the propagation paths are near-vertical (Booth and Crampin, 1985).

As remarked by Bostock et al. (2012), the P and S waveforms for the full selection of templates at a given station display remarkable uniformity across the range of epicentral distances. Furthermore, the dipolar pulses observed in the earlier study and the band-limited zero-phase pulses evident in Fig. 3 imply that the LFE templates can be considered as empirical Green's functions originating from a moment tensor point source with a step-function time dependence in displacement. Hilbert transformation of the particle velocity records is practically useful because it aids in the identification of (band-limited) arrivals for location (Section 5) and for waveform matching as required in moment tensor inversion (Section 6) and recovery of structure from scattered waves (Nowack and Bostock, 2013).

The assertion that LFE templates produced by the iterative correlation–detection–stacking procedure can be considered as empirical Green's functions can be further justified as follows. Consider the single-channel cross-correlation $c(t)$ of a (e.g. band-limited) Green's function estimate $\hat{g}(t)$ with a seismogram $u(t)$ that is itself the convolution of a source $s(t)$ with the corresponding true Green's function $g(t)$:

$$c(t) = \hat{g}(t) \otimes u(t) = \hat{g}(t) \otimes g(t) \star s(t) = \hat{\Phi}^{g}(t) \star s(t),$$

where $\otimes$ and $\star$ denote correlation and convolution, respectively. $\hat{\Phi}^{g}(t)$ is an estimate of the true autocorrelation of $g(t)$ and so will peak near lag $t = 0$. The timing of the maximum (or maxima) of $c(t)$ will depend on $s(t)$ but, owing to the timing of maximum in $\hat{\Phi}^{g}(t)$, will occur at or near the time(s) at which $s(t)$ possesses its maximum (maxima), say $t = t^{\max}$. Note that $\hat{\Phi}^{g}(t)$ may contain significant subsidiary maxima at, for example, times equal to the S–P time if both P- and S-waves project onto the given channel with comparable amplitude and polarity. The contaminating influence of secondary peaks, any bias of the autocorrelation estimate maximum away from $t = 0$ and other forms of noise will be mitigated in the selection of $t^{\max}$ when the normalized cross-correlations $c(t)/\sqrt{\int \hat{g}(\tau)^2\, d\tau \int u(\tau)^2\, d\tau}$ for many channels are combined within network correlation detection (Gibbons and Ringdal, 2006; Shelly et al., 2006).

Once the detections are logged as described in Section 3.3, the stack of corresponding seismograms $u_i(t)$ for a given channel, each shifted by the corresponding detection time $t_i^{\max}$, can be written as

$$\sum_i u_i\left(t - t_i^{\max}\right) = g(t) \star \sum_i s_i\left(t - t_i^{\max}\right).$$

As the number of detections increases, the sum of band-limited source functions $s_i(t - t^{\max})$, shifted such that their maxima align but assumed to be otherwise random, will tend toward a scaled, filtered delta function. The sum of shifted $u_i(t)$ thus becomes a scaled, band-limited approximation to $g(t)$ that can be used as an improved estimate $\hat{g}(t)$ to log further detections.

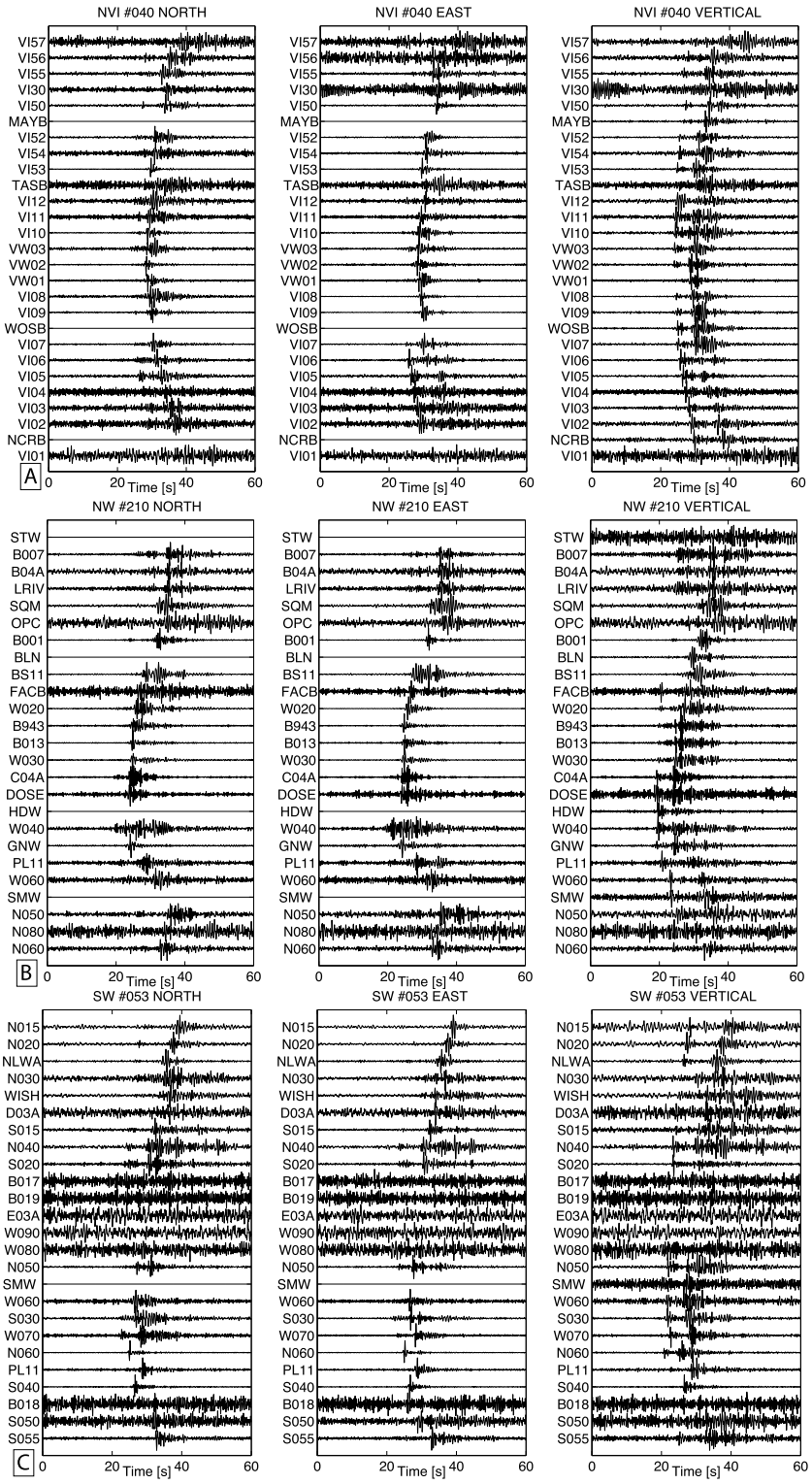

Fig. 2. North (left), east (centre) and vertical (right) components of 3 LFE templates from the (A) NVI (template 040), (B) NW (template 210) and (C) SW (template 053) subarrays.

Approximate deconvolution through stacking of phase-normalized seismograms has been applied previously to long-period body waves (Shearer, 1991) and broadband teleseismic *P*-waves (Kumar et al., 2010) using global earthquakes, however the relative infrequency of regular seismicity limits Green's function retrieval to 1-D estimates. In contrast, LFEs that repeat 1000's of times over periods of a few years allow fully 3-D empirical Green's functions to be assembled.

5. LFE template locations

A large proportion of stations represented within LFE templates display unambiguous zero-phase, impulsive *P*- and *S*-arrivals that can be timed and used to establish representative locations. We perform two locations, one using a standard linearized inversion (Hyp2000, Klein, 2002) and one using the double difference location algorithm (hypoDD, Waldhauser, 2001), both distributed by

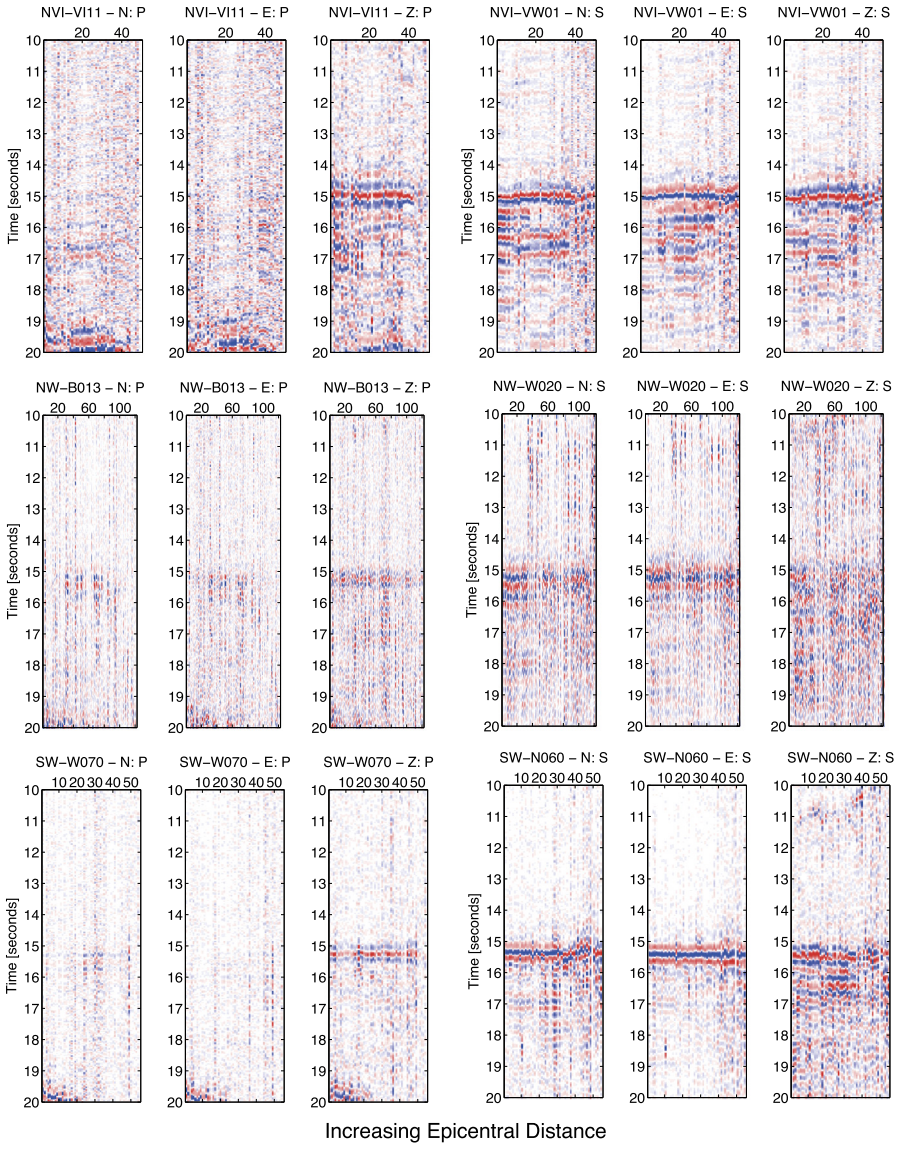

Fig. 3. Three-component LFE template waveforms for individual stations aligned on direct P/S phases and plotted as functions epicentral distance. (Top) NVI waveforms aligned on P for station VI11 and S for station VW01. (Middle) NW waveforms aligned on P for station B013 and S for station W020. (Bottom) SW waveforms aligned on P for station 2070 and S for station N060. Red/blue polarities are positive/negative, respectively. Note simple zero-phase signatures of direct P and S. (For interpretation of the references to colour in this figure legend, the reader is referred to the web version of this article.)

the United States Geological Survey. Fig. 4 shows a map of LFE Hyp2000 epicentres (see supplementary Fig. S1 for hypoDD epicentres). Superimposed on this map are the 20, 30 and 40 km depth contours to the top of the subducting Juan de Fuca plate modelled by Audet et al. (2010) and McCrory et al. (2012).

Using the initial Hyp2000 locations, we apply the hypoDD algorithm to a combination of ordinary phase picks from our LFE catalogue and differential travel times from phase correlation of P- and S-waves. The parameters used to perform the inversion are summarized in supplementary Table S1. These parameters are set to produce a dynamic weighting scheme to optimize the least-squares solution. Solutions are found by iteratively adjusting the vector difference between nearby hypocentral pairs, with the locations and partial derivatives updated after each iteration. Events lacking close neighbours are automatically removed in this procedure such that 91%, 92%, 77% and 72% of the original events remain in hypoDD solutions for the NVI, SVI, NW and SW datasets, respectively. Mean, nominal uncertainties in horizontal and vertical locations as supplied by Hyp2000 for the individual subarrays are 1.8 km, 2.16 km (NVI), 1.1 km, 1.9 km (SVI), 2.0 km, 1.3 km (NW), and 3.7 km, 3.5 km (SW).

LFE epicentres in northern Cascadia, shown in Fig. 4 and supplementary Fig. S1 fall within the general tremor epicentre distributions previously mapped by Kao et al. (2009, Figs. 7, 9) and Wech et al. (2009, Figs. 1, 3). In the southern Vancouver Island (SVI) and Washington state (NW and SW) regions, LFE epicentres are bounded by the 25 and 38 km slab depth contours for the Audet et al. (2010) model and the 32 and 45 km contours for the McCrory et al. (2012) model. In northern Vancouver Island the LFE templates map close to the 30 km contour for both models. As noted by Bostock et al. (2012) for southern Vancouver Island LFEs and by Kao et al. (2005) for tremor more generally, LFEs epicentres tend to avoid regions with higher levels of regular seismicity, shown as black dots in Fig. 4 for the period 1985–2012.

Fig. 5 plots the hypoDD locations of 10 depth profiles defined in Fig. 4 (analogous plots for the Hyp2000 locations can be found in supplementary Fig. S2). Note that A–A′ and B–B′ profiles below southern Vancouver Island were previously presented by Bostock et al. (2012). Profiles are constructed using bins

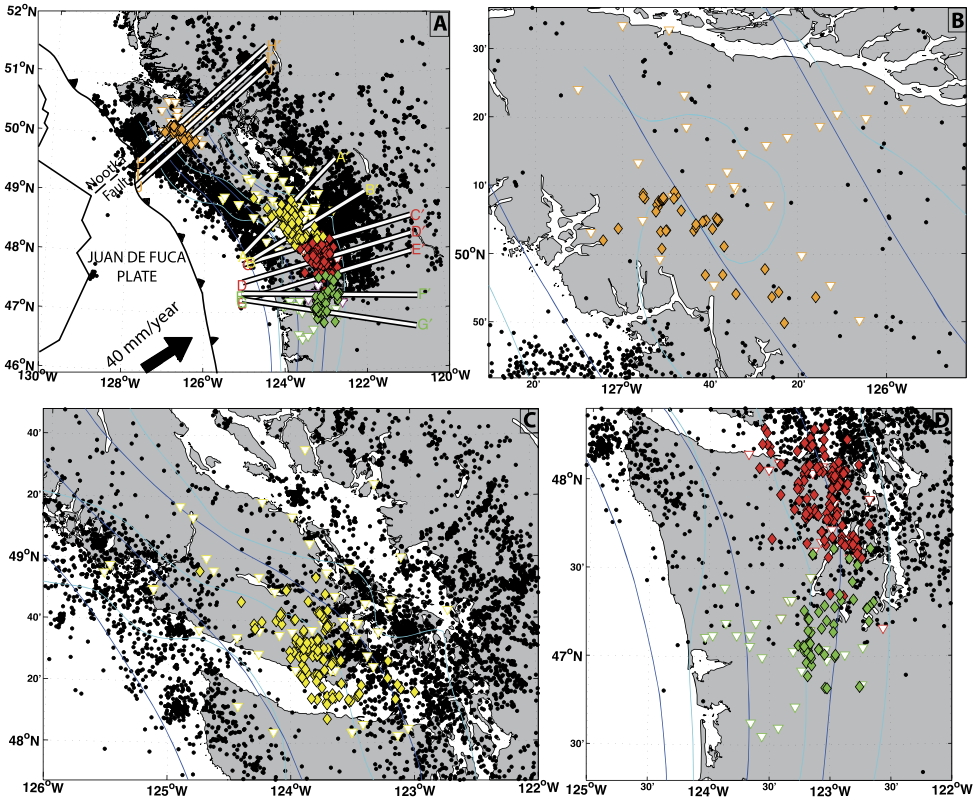

Fig. 4. Maps of LFE locations computed using the Hyp2000 software organized as in Fig. 1. Orange, red and green diamonds are LFE locations from the NVI, NW and SW arrays, respectively. Yellow diamonds are locations of LFEs in southern Vancouver Island described by Bostock et al. (2012). Cyan and blue lines indicate the 20, 30 and 40 km depth contours to the top of the subducting Juan de Fuca pate modelled by Audet et al. (2010) and McCrory et al. (2012), respectively. (For interpretation of the references to colour in this figure legend, the reader is referred to the web version of this article.)

that extend ±25 km to either side, and include the Audet et al. (2010) slab model quadratically interpolated through the 20, 30 and 40 km contours and the McCrory et al. (2012) model linearly interpolated through 5 km depth intervals between 20 and 80 km. This figure further emphasizes the segregation of LFEs from regular earthquakes. LFEs tend to lie several km on average above intraplate earthquakes where their epicentres overlap. The two slab models bracket the LFE hypocentres below southern Vancouver Island and northern Washington (profiles A, B, C), the Audet et al. (2010) model from above and the McCrory et al. (2012) model from below. Hypocentres beneath SVI range between 29 and 40 km depth whereas those below Washington state fall between 31 and 46 km depth (NW) and 32 and 49 km depth (SW). Hypocentres along the SW profiles (E, F, G) coincide more closely with the McCrory et al. (2012) model, whereas hypocentres for LFEs for NVI profiles I, J are better aligned with the Audet et al. (2010) model where hypocentres fall between 33 and 39 km depth.

6. LFE template moment tensors

In our previous effort (Bostock et al., 2012) to determine focal mechanisms of LFEs on southern Vancouver Island, we employed *P*-polarity estimates that were derived through correlation of vertical component seismograms with a reference pulse. That work suggested that LFE mechanisms comprised a mixture of thrust and strike slip faulting. We improve our analysis in the present study in several ways. First, 90° phase rotation of particle velocity seismograms provides a more robust means of producing zero-phase pulses and ascertaining the polarity of *P*- and *S*-arrivals at smaller epicentral distances than correlation with a reference pulse. Second, we have incorporated data from several previously unavailable stations along the southern coast of Vancouver Island (CPLB, LCBC, JRBC, GLBC) that significantly improve coverage in the southwestern quadrant. Finally, we now exploit the identification of the LFE templates with empirical Green's functions to perform a moment tensor inversion that, in addition to *P*-wave polarities, leverages constraints from *S*-wave polarities and relative amplitudes of both *P*- and *S*-waves.

Our moment tensor inversion procedure incorporates elements from Kikuchi and Kanamori (1991) and involves the following steps: i) each 3-component LFE template seismogram is normalized to unit, maximum absolute amplitude and phase rotated by 90° to aid in identification and picking of zero-phase, primary arrivals; ii) locations are determined from travel-time picks corresponding to those *P*- and *S*-arrivals judged to display unambiguous, zero-phase waveforms, iii) ray theoretic synthetic seismograms (Cerveny et al., 1987) comprising direct *P*- and *S*-arrivals are generated for a basis of 6 independent moment tensors and normalized/phase rotated/filtered to match the spectral properties of the data; iv) synthetic and observed *P* and *S* waveforms are aligned based on their amplitude extrema to account for unmodelled velocity structure; v) least-squares inversion is performed for the coefficients of the moment tensor basis that best explain the relative amplitudes and polarities of the primary LFE arrivals; and vi) the best double couple mechanism is extracted from the general moment tensor solution using Newton optimization.

Fig. 6 shows an example of the waveform matches derived for SVI template 005 with a double couple solution. The effect of a steeply inclined nodal plane roughly parallel to strike is evident in the change in *P*-wave polarity that occurs near station LZB and the large, negatively polarized *S*-arrivals on the north and east components at e.g., stations TWBB to PGC that straddle the plane. Best-fit double couple solutions are plotted in Fig. 7 for a geographically representative subset of SVI templates. SVI solutions are

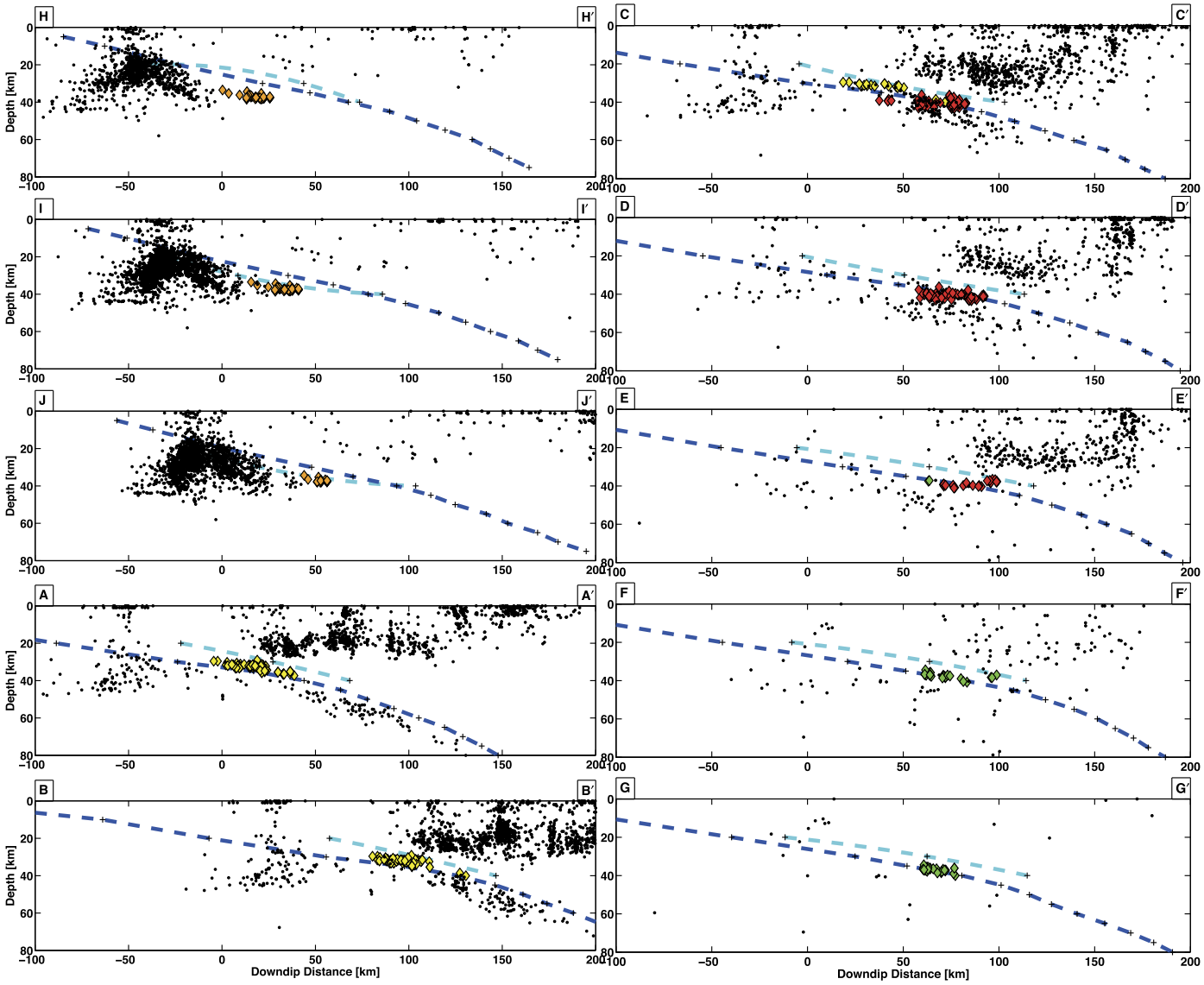

Fig. 5. Depth profiles of seismicity in Vancouver Island and Washington state. Profile locations are identified in Fig. 4A. Black dots represent regular earthquake locations for the period 1985–2012. Orange, yellow, red and green diamonds are LFE template locations determined using hypoDD for NVI, SVI, NW and SW arrays, respectively. Dashed cyan and blue lines represent depth estimates to the top of the subducting Juan de Fuca plate from the Audet et al. (2010) and McCrory et al. (2012) models, respectively. (For interpretation of the references to colour in this figure legend, the reader is referred to the web version of this article.)

generally well modelled as double couple sources as indicated by F-tests that reveal no significant improvement in fit afforded by deviatoric or full moment tensor solutions. The majority of double couple solutions are characterized by thrust mechanisms oriented in a northeasterly direction, although there are two groupings of 3–4 LFE locations each near 48.2N, 123.1W and 48.7N, 124.2 that appear to show somewhat consistent strike-slip components.

In addition to the correct identification of wavelets on LFE templates as direct *P* and/or *S*, our ability to constrain the moment tensor depends on event-station geometry as quantified by the condition number of the normal equations. The extensive areal aperture of the NVI array and a localized distribution of LFEs near its centre lead to condition numbers (mean = 17, median = 22 for the deviatoric solution, see supplementary Fig. S3) that are less than those for SVI (mean = 68, median = 33), although this measure of solution quality does not account for the template SNR that is superior for SVI. Double couple solutions for the NVI templates (Fig. 8) like those for SVI tend to be shallow thrust in nature. The same characterization holds for the SW solutions (Fig. 9) with mean and median condition numbers of 17 and 27, respectively although there is greater variability in their orientation. In contrast, moment tensor solutions for NW templates (Fig. 10) are marked by large condition numbers (mean = 366, median = 89) that manifest the quasi-linear distribution of stations, and display still greater variability in orientation. Each of Figs. 7–10 contains an inset displaying the best double couple solution (i.e. with linear vector dipole component removed) determined from the average of individual double couple solutions for all templates within the respective subarray. The corresponding averaged plate motion vector determined from data in (McCaffrey et al., 2007) is superposed on these plots. Supplementary Fig. S4 provides an alternative representation of the focal mechanism distributions as histograms of strike, rake and dip for the individual subarrays assuming that the nodal plane with shallower dip represents the fault plane.

7. Discussion and conclusions

Through the generation of LFE templates using data from EarthScope sources (Transportable Array, PBO, FlexArray), POLARIS deployments and permanent networks (CNSN, PNSN), we have ex-

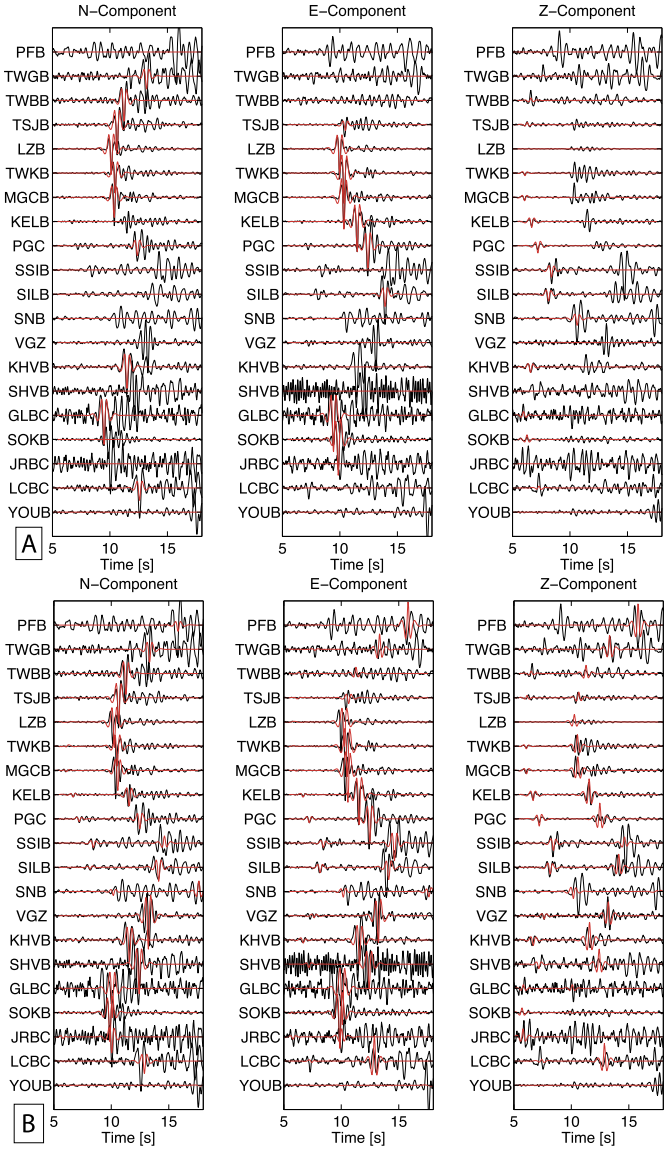

Fig. 6. Example of waveform matching in moment tensor inversion for SVI template 005. (A) Modelled data. Synthetics (red) are superimposed on data (black) for those channels selected for fitting; zero amplitude synthetic traces correspond to unused channels. *S*-waves are fit to horizontal components and *P*-waves to the vertical component with shifts up to ±0.2 s applied to maximize correlation. (B) Synthetic seismograms for full station complement corresponding to double couple solution derived from selected channels in (A). Timing misalignments result from errors in velocity model used to generate synthetics. (For interpretation of the references to colour in this figure legend, the reader is referred to the web version of this article.)

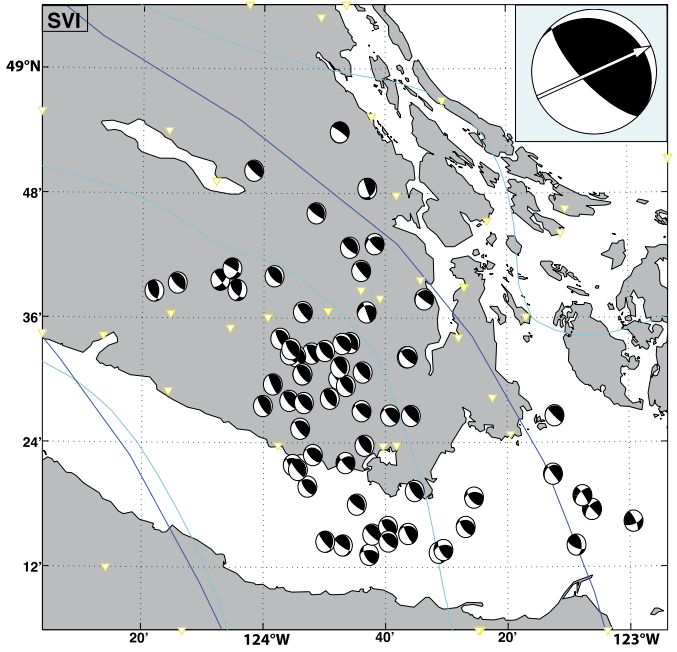

Fig. 7. Map of double couple mechanisms determined from moment tensor inversion of a selection of LFE templates from the SVI subarray. Inset shows best double couple mechanism from average over all individual moment tensors with arrow indicating corresponding averaged plate motion direction (McCaffrey et al., 2007).

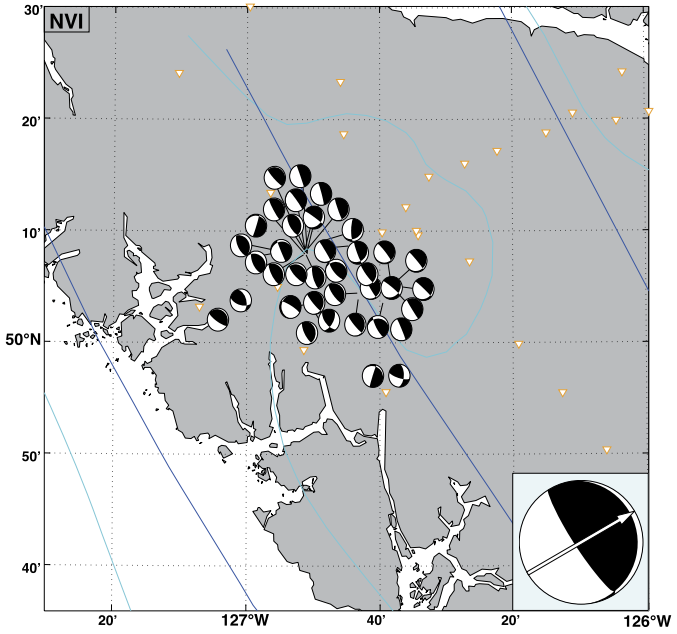

Fig. 8. Map of double couple mechanisms for NVI subarray; see caption of Fig. 7 for explanation.

tended documentation of Cascadia LFEs from southern Vancouver Island south into Washington state and north to northern Vancouver Island. Not surprisingly, LFE epicentres in northern Cascadia fall within the tremor epicentral distributions previously mapped by, e.g. Kao et al. (2009), Wech et al. (2009), and tend to avoid regions of denser, regular seismicity as reported previously for tremor (Kao et al., 2005) and for LFEs below southern Vancouver Island (Bostock et al., 2012). In particular, LFEs typically define a surface several km above the upper envelope of intraplate earthquakes and several km below the lower envelope of overlying crustal seismicity where their epicentres overlap.

LFE hypocentres generally parallel but do not coincide precisely with either of two recent models for the plate boundary in Cascadia. In fact, the hypocentres frequently locate between the plate boundary estimates, lying below the Audet et al. (2010) model and above the McCrory et al. (2012) model. The two models are based on different assumptions and data sets, and both may be subject to bias. The Audet et al. (2010) model relies on the identification of the plate boundary with the top of a pronounced low-velocity zone (LVZ) that occurs throughout Cascadia and which has been most recently interpreted to be upper oceanic crust (Hansen et al., 2012; Bostock, 2012). This model was generated for the purposes of cross-Cascadia comparisons between the geometry of the LVZ and tremor epicentral distributions (e.g. Wech and Creager, 2011, Fig. 1). It was derived using the timing of scattered teleseismic *P* phases and the simplifying assumption of a homogeneous over-

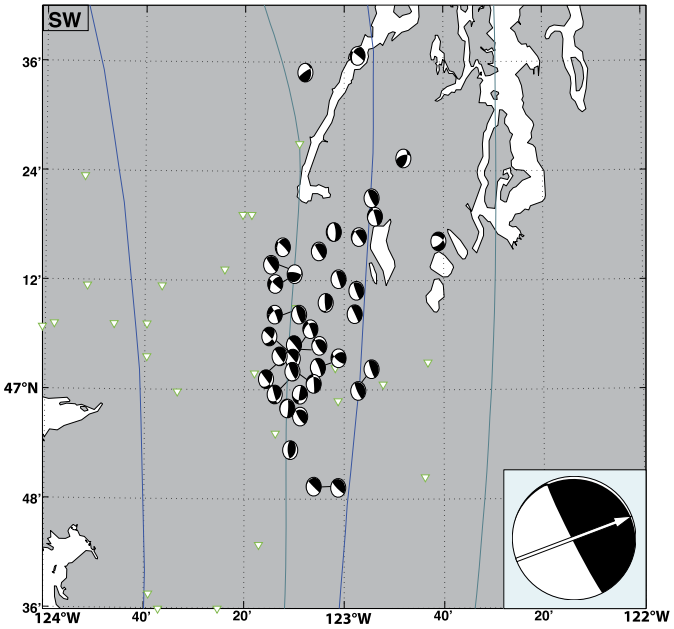

Fig. 9. Map of double couple mechanisms for SW subarray; see caption of Fig. 7 for explanation.

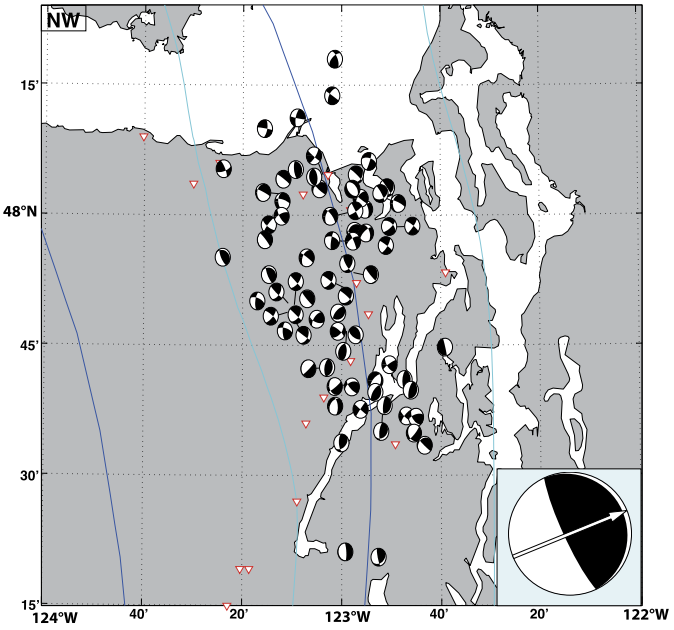

Fig. 10. Map of double couple mechanisms for NW subarray; see caption of Fig. 7 for explanation.

riding plate with fixed P-velocity of 6.5 km/s but locally variable V_P/V_S ratio as opposed to the 1-D, fixed V_P/V_S model used for LFE location. The differences in underlying velocity models may result in depth biases that are locally significant.

The McCrory et al. (2012) model was constructed by synthesizing depth information from intraplate earthquake locations and regional seismic velocity profiles. The authors inferred the top of the Juan de Fuca slab to lie near the upper surface of intraplate seismicity where present, and weighted these seismicity constraints more highly than structural information derived from velocity profiles in areas where both sources of information were available. Plate boundary depth estimates based on this approach may be biased deep by ~7 km if intraplate seismicity resides near the base of the subducting crust as has been inferred by Shelly et al. (2006) for southwest Japan. Comparison of hypocentres from southwest Japan with those from northern Cascadia (Bostock et al., 2012, Fig. 8; see also Fig. 7 and supplementary Fig. S2 herein) points to similar geometrical relations between LFEs, LVZs and intraplate seismicity, and implies that the structural controls on seismogenesis in the two regions are the same.

The only region where the Audet et al. (2010) model maps the plate boundary to deeper levels than the McCrory et al. (2012) model, is along profiles I, J in northern Vancouver Island. In this region, the Explorer microplate is interpreted to be detaching from the Juan de Fuca plate along the Nootka fault and its NE landward extension (e.g Braunmiller and Nabelek, 2002; Audet et al., 2008). The majority of LFEs here lie along a relatively flat trajectory between 35 and 38 km depth coinciding with the Audet et al. (2010) model along profiles I, J, although they lie significantly deeper than that model on profile H immediately to the north. The LFE hypocentres are also slightly deeper than the 25–35 km depths quoted for tremor in this region by Kao et al. (2009).

We have outlined simple arguments justifying the identification of LFE templates with empirical Green's functions, thereby facilitating their treatment in waveform inversions for, e.g., moment tensor solutions. Note that we do not mean to imply that all LFEs are characterized by single point source, step displacements in time. Examination of individual LFEs detected via network correlation often does reveal impulsive, albeit noisy, signals resembling the template waveforms. Just as frequently, however, the signals display more complex temporal dependencies consistent, for example, with rapid tremor streaking that has been documented in northern Washington using beamforming techniques (Ghosh et al., 2010).

Our examination of source mechanisms from the SVI subarray using moment tensor inversion improves on our analysis of P-wave polarities in Bostock et al. (2012) by including more stations from the previously poorly sampled southwestern quadrant, by employing S-wave polarities and relative amplitudes across individual station components, and by the use of a 90° phase rotation to facilitate phase identification within the band-limited signals. SVI moment tensor solutions are generally well constrained and the large majority (~90%) of mechanisms are consistent with shallow thrust faulting in the direction of relative plate motion. The variability in focal mechanisms increases progressively through the NVI, SW and NW subarrays. We suspect that this variability may be due partly to poorer station coverage (for NW in particular) and partly to lower SNR resulting from smaller numbers of contributing detections. Diminished SNR renders it difficult to accurately isolate phases, especially S, within band-limited data. S is particularly problematic because, at larger epicentral distances, generation of post-critically reflected P at the free surface significantly distorts S waveforms (Booth and Crampin, 1985) such that only the SH component retains its original source signature. In addition, strong anisotropy is known to occur in some areas (Bostock and Christensen, 2012) and may also contaminate waveforms through splitting. Notwithstanding variability in focal mechanism consistency across the different subarrays, the average double couple solution for each (see insets in Figs. 7–10) is generally consistent with shallow thrusting in the direction of plate motion.

These subarray-averaged moment tensors and the preponderance of individual thrust mechanisms for the SVI, NVI (and to a lesser extent SW) subarrays approximately aligned with the plate motion direction leads us to suspect that shallow thrust faulting may prevail throughout the northern Cascadia region, as has been argued for SW Japan by Ide et al. (2007) and central Mexico by Frank et al. (2013). In so doing, we interpret variability in focal mechanisms in Figs. 7–10 (for the NW array in particular) as due to variations in SNR and conditioning of the inverse problem.

We acknowledge, however, the possibility that, locally, LFE mechanisms may depart from the shallow thrust orientation dependent, for example, upon structure in the downgoing plate. The likelihood that a majority of, if not all, LFE mechanisms are shallow thrust would weaken the argument by Bostock et al. (2012) that LFEs are distributed through a plate boundary shear zone coinciding with the (3–4 km thick) LVZ. Although our nominal depth location uncertainties ($\sim\pm2$ km) do not allow us to address this issue directly, recent work by (Nowack and Bostock, 2013) employing scattered waves from a selection of templates requires LFEs to occur <1 km below the top of the LVZ. This constraint together with the moment tensor results presented here are consistent with an origin for LFEs as shear slip along a relatively sharp plate boundary atop the LVZ.

Acknowledgements

We gratefully acknowledge the constructive criticisms of two anonymous referees that led to improvements in the final manuscript. This research was supported by the Natural Sciences and Engineering Research Council of Canada Discovery Grant RGPIN 138004.

Appendix A. Supplementary material

Supplementary material related to this article can be found online at http://dx.doi.org/10.1016/j.epsl.2013.08.040.

References

Abers, G.A., MacKenzie, L.S., Rondenay, S., Zhang, Z., Wech, A.G., Creager, K.C., 2009. Imaging the source region of Cascadia tremor and intermediate-depth earthquakes. Geology 37, 1119–1122. http://dx.doi.org/10.1130/G30143A.1.

Audet, P., Bostock, M.G., Boyarko, D.C., Brudzinski, M.R., Allen, R.M., 2010. Slab morphology in the Cascadia forearc and its relation to episodic tremor and slip. J. Geophys. Res. 115, B00A16. http://dx.doi.org/10.1029/2008JB006053.

Audet, P., Bostock, M.G., Mercier, J.P., Cassidy, J.F., 2008. Morphology of the Explorer–Juan de Fuca slab edge in northern Cascadia: Imaging plate capture at a ridge-trench-transform triple junction. Geology 36, 895–898. http://dx.doi.org/10.1130/G25356A.1.

Booth, D.C., Crampin, S., 1985. Shear wave polarization on a curved wavefront at an isotropic free surface. Geophys. J. R. Astron. Soc. 83, 31–45.

Bostock, M.G., 2012. The Moho in subduction zones. Tectonophysics. http://dx.doi.org/10.1016/j.tecto.2012.07.007.

Bostock, M.G., Christensen, N.I., 2012. Split from slip and schist: Crustal anisotropy beneath northern Cascadia from non-volcanic tremor. J. Geophys. Res. 117, B08303. http://dx.doi.org/10.1029/2011JB009095.

Bostock, M.G., Royer, A.A., Hearn, E.H., Peacock, S.M., 2012. Low frequency earthquakes below southern Vancouver Island. Geochem. Geophys. Geosyst. 13, 11. http://dx.doi.org/10.1029/2012GC004391.

Braunmiller, J., Nabelek, J., 2002. Seismotectonics of the Explorer region. J. Geophys. Res. 107. http://dx.doi.org/10.1029/2001JB000220.

Brown, J.R., Beroza, G.C., Shelly, D.R., 2008. An autocorrelation method to detect low frequency earthquakes within tremor. Geophys. Res. Lett. 38, L16305. http://dx.doi.org/10.1029/2008JL034560.

Calkins, J.A., Abers, G.A., Ekström, G., Creager, K.C., Rondenay, S., 2011. Shallow structure of the Cascadia subduction zone beneath western Washington from spectral ambient noise correlation. J. Geophys. Res. 116, B07302. http://dx.doi.org/10.1029/2010JB007657.

Cerveny, V., Klimes, L., Psencik, I., 1987. Complete seismic ray tracing in complex 3-d structures. In: Doornbos, D. (Ed.), Seismological Algorithms. Academic Press, New York, pp. 89–168.

Frank, W.B., Shapiro, N.M., Kostoglodov, V., Husker, A.L., Campillo, M., Payero, J.S., Prieto, G.A., 2013. Low-frequency earthquakes in the Mexican Sweet Spot. Geophys. Res. Lett. 40, 2661–2666. http://dx.doi.org/10.1002/grl.50561.

Ghosh, A., Vidale, J.E., Sweet, J., Creager, K.C., Wech, A., Houston, H., Brodsky, E., 2010. Rapid, continuous streaking of tremor in Cascadia. Geochem. Geophys. Geosyst. 11. http://dx.doi.org/10.1029/2010GC003305.

Gibbons, S.J., Ringdal, F., 2006. The detection of low magnitude seismic events using array-based waveform correlation. Geophys. J. Int. 165, 149–166. http://dx.doi.org/10.1111/j.1365-246X.2006.02865.x.

Hansen, R.T.J., Bostock, M.G., Christensen, N.I., 2012. Nature of the low velocity zone in Cascadia from receiver function waveform inversion. Earth Planet. Sci. Lett. 337–338, 25–38. http://dx.doi.org/10.1016/j.epsl.2012.05.031.

Ide, S., Shelly, D.R., Beroza, G.C., 2007. Mechanism of deep low frequency earthquakes: Further evidence that deep non-volcanic tremor is generated by shear slip on the plate interface. Geophys. Res. Lett. 34, L03308. http://dx.doi.org/10.1029/2006GL028890.

Kao, H., Shan, S.J., Dragert, H., Rogers, G., 2009. Northern Cascadia episodic tremor and slip: A decade of tremor observations from 1997 to 2007. J. Geophys. Res. 114. http://dx.doi.org/10.1029/2008JB006046.

Kao, H., Shan, S.J., Dragert, H., Rogers, G., Cassidy, J.F., Ramachandran, K., 2005. A wide depth distribution of seismic tremors along the northern Cascadia margin. Nature 436, 841–844. http://dx.doi.org/10.1038/nature03903.

Kikuchi, M., Kanamori, H., 1991. Inversion of complex body waves – III. Bull. Seismol. Soc. Am. 81, 2335–2350.

Klein, F.W., 2002. User's Guide to HYPOINVERSE-2000, a Fortran Program to Solve for Earthquake Locations and Magnitudes. U.S. Geol. Surv. Open File Rep. 02-171.

Kumar, P., Kind, R., Yuan, X., 2010. Receiver function summation without deconvolution. Geophys. J. Int. 180, 1223–1230. http://dx.doi.org/10.1111/j.1365-246X.2009.04469.x.

McCaffrey, R.A., Qamar, A., King, R., Wells, R., Khazaradze, G., Williams, C., Stevens, C., Vollick, J., Zwick, P., 2007. Fault locking, block rotation and crustal deformation in the Pacific Northwest. Geophys. J. Int. 169, 1315–1340. http://dx.doi.org/10.1111/j.1365-246X.2007.03371.x.

McCrory, P.A., Blair, J.L., Waldhauser, F., Oppenheimer, D.H., 2012. Juan de Fuca slab geometry and its relation to Wadati–Benioff zone seismicity. J. Geophys. Res. 117, B09306. http://dx.doi.org/10.1029/2012JB009407.

Nowack, R.L., Bostock, M.G., 2013. Scattered waves from low frequency earthquakes and plate boundary structure in northern Cascadia. Geophys. Res. Lett. 40. http://dx.doi.org/10.1002/grl.50826.

Obara, K., 2002. Nonvolcanic deep tremor associated with subduction in southwest Japan. Science 296, 1679–1681. http://dx.doi.org/10.1126/science.1070378.

Rogers, G., Dragert, H., 2003. Episodic tremor and slip on the Cascadia subduction zone: The chatter of silent slip. Science 300, 1942–1943. http://dx.doi.org/10.1126/science.1084783.

Rowe, C.A., Aster, R.C., Borchers, B., Young, C.J., 2002. An automatic, adaptive algorithm for refining phase picks in large seismic data sets. Bull. Seismol. Soc. Am. 92, 1660–1674. http://dx.doi.org/10.1785/0120010224.

Shearer, P.M., 1991. Imaging global body wave phases by stacking long-period seismograms. J. Geophys. Res. 96, 20353–20364. http://dx.doi.org/10.1029/91JB00421.

Shelly, D.R., Beroza, G.C., Ide, S., 2007. Non-volcanic tremor and low-frequency earthquake swarms. Nature 446, 305–307. http://dx.doi.org/10.1038/nature05666.

Shelly, D.R., Beroza, G.C., Ide, S., Nakamura, S., 2006. Low-frequency earthquakes in Shikoku, Japan, and their relationship to episodic tremor and slip. Nature 442, 188–191. http://dx.doi.org/10.1038/nature04931.

Shelly, D.R., Hardebeck, J.L., 2010. Precise tremor source locations and amplitude variations along the lower-crustal central San Andreas Fault. Geophys. Res. Lett. 37. http://dx.doi.org/10.1029/i2010GL043672.

Waldhauser, F., 2001. hypoDD – A Program to Compute Double-Difference Hypocenter Locations. U.S. Geol. Surv. Open File Rep. 1-113.

Wech, A.G., Creager, K.C., 2011. A continuum of stress, strength and slip in the Cascadia subduction zone. Nat. Geosci. 4, 624–628. http://dx.doi.org/10.1038/ngeo1215.

Wech, A.G., Creager, K.C., Melbourne, T.I., 2009. Seismic and geodetic constraints on Cascadia slow slip. J. Geophys. Res. 114. http://dx.doi.org/10.1029/2008JB006090.